Research article

JGS
Journal of the Geological Society

https://doi.org/10.1144/jgs2022-036 | Vol. 180 | 2023 | jgs2022-036

Crystal entrainment from cool, low-silica rocks into hot, high-silica melts: diverse primary melt compositions at Taranaki volcano, New Zealand

Nessa G. D'Mello[1]*, Georg F. Zellmer[1], Gabor Kereszturi[1], Teresa Ubide[2], Jonathan N. Procter[1] and Robert B. Stewart[1]

[1] VRS, School of Agriculture and Environment, Massey University, Palmerston North, New Zealand 4410
[2] School of Earth and Environment Sciences, The University of Queensland, Brisbane, QLD 4072, Australia
NGD, 0000-0001-5627-528X
* Correspondence: n.dmello@massey.ac.nz

Abstract: The prevalence of antecrysts in arc volcanic rocks is widely accepted, yet the origin of their carrier melts remains debated. Crystal cargo in lava flows from Taranaki volcano, New Zealand, is dominated by plagioclase, clinopyroxene and amphibole. Except for some crystal rims, mineral phases are in disequilibrium with the melt they are entrained in. Major element chemistry reveals an almost complete compositional overlap between the crystals in the lava and those in xenoliths. The large volume fraction of crystals (35–55 vol%) exerts a strong control on whole-rock compositions, reducing silica by 5–11 wt% compared with the carrier melt. Yet there is no clear relationship between mineral proportion and bulk-rock compositions. Our data are inconsistent with extensive fractional crystallization, commonly invoked as a driver of magma evolution towards silica-rich compositions. Instead, high-temperature, aphyric carrier melts with varied compositions (55–68 wt% SiO_2) entrain crystal cargo while ascending through colder, low-silica rocks. Thus, some parental melts at Taranaki volcano are significantly more silica-rich than arc basalts commonly invoked as primary magmas. Further, thermometric and hygrometric constraints preclude a deep crustal hot zone for the source of these melts, which we argue are of subcrustal origin.

Supplementary material: Supplementary figures and databases are available at https://doi.org/10.6084/m9.figshare.c.6406813

Received 4 March 2022; **revised** 18 January 2023; **accepted** 19 January 2023

Volcanic rocks of intermediate composition (52–63 wt% SiO_2; Le Maître 2002) make up a significant proportion of arc volcanism and are representative of the bulk composition of the continental crust (Gill 1981). Constraining their petrogenesis is critical to understanding the evolution of the crust, as well as the assessment of volcanic hazards at subduction zones. Intermediate magmas are conventionally viewed as originating from primary basaltic melts, released from the mantle into the overlying crust, where they are thought to evolve in polybaric (mid- to lower-crustal) storage regions (e.g. Grove and Donnelly-Nolan 1986; Cashman and McConnell 2005; Davidson *et al.* 2005; Melekhova *et al.* 2014). There, they are subject to fractional crystallization and interactions with crustal rocks, crystal mushes, plutonic intrusive rocks and freshly injected melt batches, ultimately resulting in an array of melt compositions (e.g. Hildreth and Moorbath 1988; Annen *et al.* 2006; Solano *et al.* 2012).

Alternatively, recent research suggests that melt differentiation can occur in the mantle wedge through incorporation of crustal (eroded forearc) and sedimentary components into the subduction channel, forming high-silica mélanges (e.g. Straub *et al.* 2020). Such mélanges may undergo diapiric upwelling from the subducted plate and react with the peridotitic mantle wedge, forming low- or high-silica pyroxenites depending on the proportion of mélange components (Behn *et al.* 2011; Straub *et al.* 2011; Nielsen and Marschall 2017). Partial melts of these lithologies are thought to be bimodal in composition (basaltic and dacitic), and their hybridization at sub-crustal depth may yield high-Mg# andesitic magmas (Straub *et al.* 2011). Further, direct melting of the inner, unreacted parts of subduction mélange diapirs at subcrustal depths may result in the generation of low-Mg# high-silica melts (Straub *et al.* 2020).

The mélange diapir model implies that the role of fractional crystallization in the evolution of arc magmas may be less pronounced than traditionally considered. Arc magmas contain a significant proportion of crystals with disequilibrium textures, which record variations in magmatic conditions and open-system magmatic evolution (Gill 1981; Zellmer *et al.* 2016). The origin of phenocrysts (here used as the original, purely textural term referring to crystals larger than the rock groundmass (Iddings 1892)) is varied. Following the terminology of Zellmer (2021), these crystals may be autocrystic (i.e. crystallized from the melt they are entrained in), xenocrystic (i.e. foreign to the magmatic host and magma system) or antecrystic (i.e. recycled within the present-day magmatic system before inclusion in the host magma). In contrast, groundmass microlites that crystallize during ascent, eruption or post-eruption are typically autocrystic, although the presence of antecrystic microlites has also been reported (Lormand *et al.* 2021). The presence of antecrysts and xenocrysts can significantly affect whole-rock compositions and thus bias petrogenetic interpretations of whole-rock data (Larrea *et al.* 2013; Ubide *et al.* 2014*b*).

In this study, we investigate the young, exposed suite of porphyritic, high-K rocks from Taranaki volcano, New Zealand, to understand differentiation processes in arc magmas. Taranaki's young lava flow samples are the least altered volcanic rocks, and thus will offer the best insights into primary magmatic processes operating at this edifice in the Holocene. The lava flows extruded over the last 7000 years have compositions that range from basalt to trachyandesite. They carry a complex crystal cargo as well as a variety of plutonic xenoliths. We apply detailed petrography as well as whole-rock, groundmass and phenocryst chemistry, thermobarometry and hygrometry, and compare our results with geochemical data from xenoliths in the region. Our dataset provides an ideal suite to elucidate the origin of intermediate compositions in an active back-arc subduction setting.

Geological background

Volcanism in the North Island of New Zealand results from the subduction of the Pacific plate beneath the Australian plate along the Hikurangi margin (Ballance 1976) (Fig. 1a). The westernmost expression of volcanism in the North Island of New Zealand is along the Taranaki Volcanic Lineament (Fig. 1b), which comprises three onshore volcanoes: Kaitake (0.57 Ma), Pouakai (0.25 Ma) and the youngest and the only active volcano, Taranaki (Neall 1979). The present-day edifice of Taranaki has a central summit vent and a satellite vent on the southern flank of the volcano, called Fanthams' Peak or Panitahi.

Taranaki volcano lies 140 km west of the Taupo Volcanic Zone, *c.* 400 km west of the Hikurangi Trough and *c.* 180 km above the Wadati–Benioff Zone (Locke *et al.* 1994; Stewart *et al.* 1996). The volcano overlies *c.* 35 km thick continental crust characterized by a normal heat flow (Price *et al.* 1999), with maximum depth of main seismicity at 25 km, although rare seismic events occur below the volcano at *c.* 600 km depth (Boddington *et al.* 2004). Cronin *et al.* (2021) summarized the crust–mantle interface beneath Taranaki based on geophysical studies and geochemical analyses of xenoliths. Hypotheses for the generation of magmas at Taranaki have attributed them to mantle corner flow (Price *et al.* 1992; Reyners *et al.* 2006), lithospheric mantle instability (Stern *et al.* 2006, 2010) and crustal delamination (Dimech *et al.* 2017). Magmatic activity at Taranaki has also been attributed to the propagation of the Taranaki Basin (Sherburn and White 2005; Sherburn *et al.* 2006; Giba *et al.* 2010).

The basement of the volcano comprises sediments of the Taranaki basin, plutonic rocks of the Median Batholith and metamorphic rocks of the deeper crust (Mortimer *et al.* 1997; Price *et al.* 2016). The present stratocone was constructed over the last *c.* 7 kyr and represents only a small percentage of the volume of material extruded from the volcano (Price *et al.* 1999, 2021). Taranaki's full volcanic history spans <200 kyr and is marked by repeated cone collapse and regrowth episodes (Procter *et al.* 2009; Zernack and Procter 2021). Sector collapses might have been triggered by eruptions, shallow-level intrusions, cone instabilities or regional earthquakes (Zernack *et al.* 2009). Edifice reconstruction followed, with eruptions generating explosive to effusive volcanic products (Platz *et al.* 2006; Platz 2007; Turner *et al.* 2008, 2009*a*, 2011; Damaschcke *et al.* 2017). Taranaki early eruptions now form an extensive ring plain deposit surrounding the peak (Zernack *et al.* 2011).

The oldest exposed lavas of the present-day edifice are the Warwick Castle Lavas (7 ka), which were partially eroded through flank collapse (*c.* 7–5 ka). This was followed by the emplacement of the Peters lava (7–3.3 ka). Contemporaneous activity at the summit vent and Fanthams Peak (*c.* 7–0.5 ka) resulted in the eruption of tephras and lavas at Fanthams Peak (F1, F2, F3) and the Staircase, and McKays Flows from the summit, along with the emplacement of lava domes (Stewart *et al.* 1996; Zernack *et al.* 2011). This

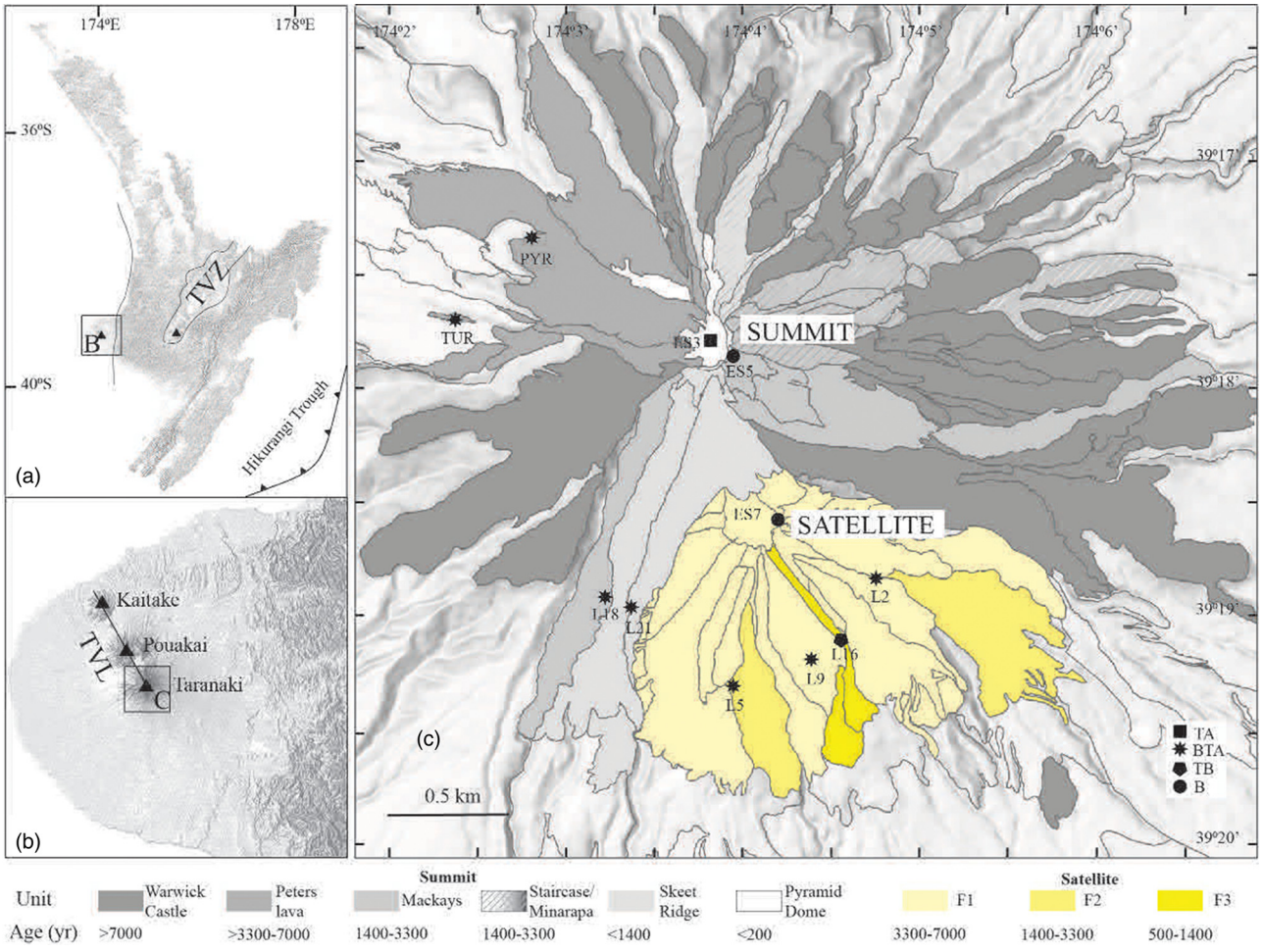

Fig. 1. (**a**) Regional geology of the North Island of New Zealand showing the primary zone of subduction (Hikurangi Trough) and the location of the Taupo Volcanic Zone (TVZ). (**b**) Taranaki Volcanic Lineament (TVL) comprising three onshore peaks: Kaitake, Pouakai and Taranaki. (**c**) Lava flows of Taranaki from the summit vent (grey) and satellite vent (yellow). Sample locations marked with symbols according to whole-rock compositions: TA, trachyandesite; BTA, basaltic trachyandesite; TB, trachybasalt; B, basalt. (Modified from Neall *et al.* 1986; King and Thrasher 1996; Torres-Orozco *et al.* 2017.)

activity was followed by the eruption of the Skeet Ridge lavas from the summit, which bifurcated around the satellite cone, and the Minarapa Lavas flowing towards the north between 3.3 and <1.4 ka (Stewart *et al.* 1996). The most recent activity, <200 years ago, involved the emplacement of a summit dome named Pyramid Dome (Lerner *et al.* 2019).

Methods

Sampling and preliminary characterization

Volcanic rocks were collected from multiple locations on Taranaki volcano, representing different eruptive phases of the present-day cone (Fig. 1c). Although the samples represent only the youngest lavas of a *c.* 200 kyr old volcanic system, they are the least altered samples and can be used for accurate geochemical analyses. The rocks were cut to expose fresh surfaces, then used for thin section preparation and back-scattered electron (BSE) imaging. Petrographic thin sections were studied using FEI 200 Quanta Scanning electron microscopy–energy-dispersive spectroscopy (SEM-EDS) to identify and image mineral populations. We used an accelerating voltage of 20 kV and a working distance of 10 mm. Semi-quantitative spot analyses were conducted using Genesis EDAX software, measuring Ca, Al, Mg and Si. BSE images were imported into the Fiji ImageJ software and adjusted for contrast and brightness. Of all samples, we selected 11 as representative of the lithological and stratigraphic variety in the present-day edifice. Crystal populations of this subset of samples were further investigated and categorized based on textures and zoning patterns observed in the BSE images. Eighty representative crystals were analysed for major and minor element chemistry, with a total of 596 data points (241 for plagioclase, 217 for clinopyroxene and 138 for amphibole crystals).

Petrography and modal abundances

To quantify modal abundances of phenocrysts in each sample, we took thin section photomicrographs at ×2.5 magnification using a Nikon Eclipse Ci POL upright microscope with an attached camera. Heterogeneity in modal abundance of mineral phases owing to large crystal sizes and their random distribution was minimized by considering 10 photographs per sample. The crystals were manually outlined and coloured, avoiding crystals <80 μm in length. Images were then imported into Adobe Photoshop, stitched and a composite mosaic was obtained. The sum area of each mineral phase, glass or vesicle was obtained using the measure tool in ImageJ. The area percentages were then used to calculate the modal abundances of each mineral phase and groundmass (glass + microlites), on a vesicle-free basis.

X-ray fluorescence (XRF) whole-rock analysis

Approximately 10 g of unaltered material from each sample was cleaned in an ultrasonic bath and dried overnight in an oven at 100°C. The samples were ground using a tungsten carbide mill and left in an oven at 110°C for at least 2 h. Loss on ignition (LOI) was calculated from the difference in weight of *c.* 2 g of the sample before and after being placed in a muffle furnace at *c.* 900°C for 8 h. Fused glass discs were prepared by mixing 0.800 g (±0.001 g) of sample powder with 8.000 g (±0.001 g) of lithium tetraborate–lithium metaborate (12:22) X-ray flux, followed by fusion with a XRFuse2 electrical fusion apparatus at Massey University, New Zealand. Glass beads were then analysed for major element concentrations using a Bruker S8 Tiger Series II WD-XRF Spectrometer at Massey University. Oreas 24b and Oreas 24c Certified Reference Materials were used as working standards. Analytical precision (1σ) was <1.5% and accuracy was within 1–3% (within 4% for TiO_2).

Laser ablation inductively coupled plasma mass spectrometry (LA-ICP-MS) whole-rock analysis

Whole-rock powders previously fused to form glass discs were used for analysis of 35 minor and trace elements at the University of Waikato, New Zealand. Spot-measurements were carried out on pre-ablated samples to remove surface particles. The instrument used was a RESOlution-SE compact 193 nm excimer laser ablation system, coupled with an Agilent 8900 triple-quadrupole mass spectrometer, using National Institute of Standards and Technology Standard Reference Material (NIST SRM) 612 as a primary standard and NIST SRM 610 as a secondary standard. Spot size was 100 μm, with laser voltage of 0.89 kV, laser energy of 4.5 mJ and fluence of *c.* 5 J cm^{-2}. Precision was typically between 1 and 10% and accuracy between 1 and 12% for minor and trace elements.

Electron probe microanalysis (EPMA)

In situ major element analyses were carried out at the Victoria University of Wellington using a JXA-8230 SuperProbe Microanalyser. EPMA was conducted using a focused beam (1–5 μm) at 20 kV accelerating voltage and 12 nA beam current for analysis of phenocrysts, and a defocused beam (30 μm) at 20 kV accelerating voltage and 8 nA beam current for groundmass analysis. The groundmass analysis included microlites and glass, with an average of 35 spot measurements per sample to avoid errors arising from the abundance of microlites in the groundmass. Phenocryst data were collected at 10–100 μm intervals along core to rim transects depending on the size of the crystal. The instrument was calibrated using a variety of mineral, glass and oxide standards (following Jarosewich *et al.* 1980) optimized for the minerals of interest. Counting times were 30 and 15 s for peak and background for all elements except Na in groundmass, which was counted for 10 and 5 s. A maximum relative precision of 1.5% and accuracy of 5% were obtained for all major oxides, based on concurrent measurement on secondary standards of the same minerals.

Results

Whole-rock and groundmass chemistry

The 45 samples investigated comprise basalts, trachybasalts, basaltic trachyandesites and trachyandesites, and range from dense to scoriaceous lava samples. The sampled lavas are relatively high in potassium (1.55–2.81 wt% K_2O) and range from basalts to trachyandesites in the total alkali–silica (TAS) classification of Le Maître (2002). Within the dominant basaltic trachyandesite group (Fig. 2a and Supplementary data SD1) there is a large compositional overlap between summit and satellite vents. However, the summit rocks are overall richer in silica. Occasionally, basalts have also erupted from the summit (e.g. sample ES5). In the present study, we follow IUGS code and refer to compositions as ultrabasic (<45 wt% SiO_2), basic (45–52 wt% SiO_2), intermediate (52–63 wt% SiO_2) and acid (>63 wt% SiO_2). Silica abundances for the entire sample suite range from 49.4 to 57.1 wt%, thus classifying as basic to intermediate. The rocks have relatively low Mg# (Mg# = 100 × molar MgO/(MgO + total FeO)), ranging from 28.4 to 34.2. Samples from the summit and satellite vents show similar major element trends, decreasing in TiO_2, $Fe_2O_3^t$, CaO and MgO and increasing in SiO_2, Al_2O_3 and Na_2O as K_2O increases (see Supplementary data SD1 and Supplementary Fig. 1).

Ni and Cr concentrations in Taranaki lavas are relatively low, rarely exceeding 20 and 50 ppm, respectively. Large ion lithophile elements (LILE) and light rare earth elements (LREE) are

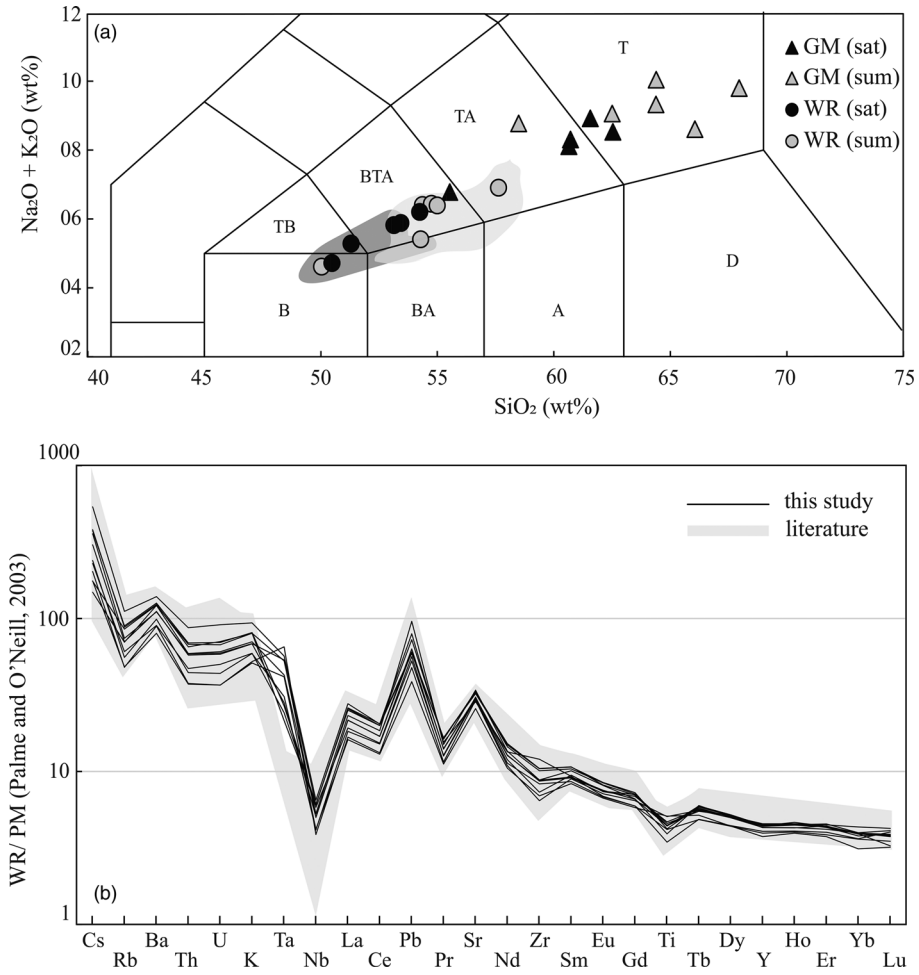

Fig. 2. (**a**) Total alkali v. silica classification (Le Maître 2002) of whole-rock (WR) and groundmass data (GM, including microlites and glass) for the investigated Taranaki samples (B, basalt; BA, basaltic andesite; A, andesite; TB, trachybasalt; BTA, basaltic trachyandesite; TA, trachyandesite; T, trachyte; D, dacite). (**b**) Primitive Mantle normalized (after Palme and O'Neill 2003) multi-elemental plots for Taranaki WR samples from this study and from the literature (Price *et al.* 1992, 1999; Stewart *et al.* 1996; Zernack *et al.* 2012). sat, satellite vent; sum, summit vent.

abundant, with Ba concentrations ranging from 560 to 970 ppm and Sr concentrations from 544 to 717 ppm. Primitive mantle normalized multi-element patterns show features characteristic of subduction-related volcanic rocks, with depletions in fluid-immobile high field strength elements such as Nb, Ti and Zr, and enrichments in fluid-mobile LILE such as K, Cs and Ba (Fig. 2b) (Stewart *et al.* 1996).

Major element data for the groundmass (glass + microlites) show compositions ranging from basaltic trachyandesites to trachydacites (*c.* 55–70 wt% SiO_2). Groundmass compositions reflect differences between satellite and summit lavas, with the satellite groundmass compositions being poorer in silica in relation to the summit lavas. Supplementary Figure S1 shows the higher silica and alkali content of the groundmass with respect to the whole-rock compositions, which yield higher MgO, $Fe_2O_3^t$ and TiO_2.

Petrography and mineral chemistry

The samples display porphyritic textures with variable proportions of large crystals (phenocrysts), sometimes assembled into glomerocrysts, hosted in a microlite-rich groundmass. No clear distinction can be made between samples from the summit and the satellite vents. Owing to the large crystal sizes and the presence of glomerocrysts, the distribution of crystals is highly heterogeneous among thin sections of the same sample. The mineral assemblage is composed of plagioclase, pale pink to green clinopyroxene, brown amphibole, opaque minerals (mostly Fe–Ti oxides), orthopyroxene and occasional olivine. Accessory phases include biotite and apatite. The groundmass microlites include dominant plagioclase, clinopyroxene, and opaque minerals with interstitial glass. Glomerocrysts include clinopyroxene crystals intergrown with each other, clinopyroxene and plagioclase, and clinopyroxene and amphibole crystals (Fig. 3a and b). Phenocrysts are commonly fractured (Fig. 3c and d). Following the crystal size classification of Zellmer (2021), the phenocryst population can be divided into mesocrysts (100–500 μm in length) and macrocrysts (500 μm–10 mm), with percentage areas varying from *c.* 35 to 55% vol% (Fig. 3f). The mineral chemistry of the phenocrysts is reported in the Supplementary data along with additional petrographic images (Supplementary Fig. S3). Although numerous glomerocrysts and microcrysts (≥30 μm in width and <100 μm in length), as well as microlites (<30 μm in width), are observed in the rocks, the present mineral chemical work focuses on the analysis of phenocryst populations that are >100 μm in length (i.e. mesocrysts and macrocrysts).

The phenocryst mineralogy of Taranaki lavas is dominated by plagioclase, clinopyroxene and, in some samples, amphibole. Plagioclase is the most abundant mineral phase, ranging from 25 to 45 vol% (see Supplementary data), with compositions ranging from An_{92} to An_{40} ($An = 100 \times$ molar $Ca/(Ca + Na + K)$) in different crystals (Supplementary Fig. S2A). The microcrysts are generally euhedral, whereas the larger crystals are often subhedral to subrounded with sieve textures showing complex zoning patterns in BSE images. Clinopyroxene modal proportions vary from 5 to 20 vol%. Crystals are weakly pleochroic from green to pink. They classify as diopsides and augites (Morimoto 1988) (Supplementary Fig. S2B) and usually contain opaque inclusions. Clinopyroxene commonly occurs as zoned, euhedral macrocrysts, and as large crystal clots with complex zoning patterns. Clinopyroxene phenocrysts have Mg# between 70 and 50, and relatively constant calcium content (*c.* 20 wt% CaO). Amphibole, when present, makes up <1 to 5.5 vol% of the rock and classifies as

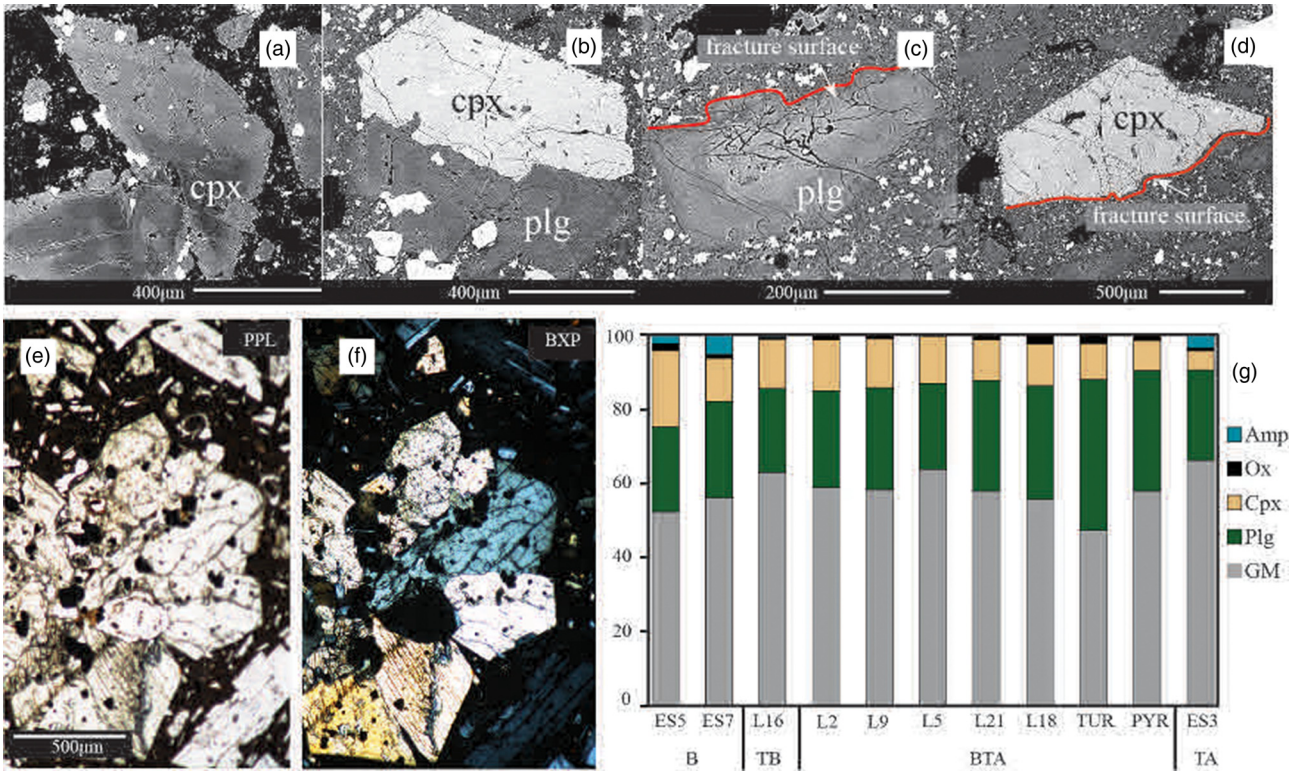

Fig. 3. Mineral textures and compositions in the investigated Taranaki rocks. Representative SEM-BSE images: (**a**) clinopyroxene in sample TUR; (**b**) intergrowth of clinopyroxene and plagioclase phenocrysts in sample L2; (**c**, **d**) fractured crystals of plagioclase and clinopyroxene in sample L18; (**e**, **f**) clinopyroxene-dominated glomerocryst in plane-polarized light (PPL; **e**) and in cross-polarized light (BXP; **f**). (**g**) Modal abundances of phenocryst phases (mesocryst and macrocryst) and groundmass in each sample, grouped by whole-rock composition. Amp, amphibole; Ox, Fe–Ti oxides; Cpx, clinopyroxene; Plg, plagioclase; GM, groundmass; B, basalt; TB, trachybasalt; BTA, basaltic trachyandesite; TA, trachyandesite.

pargasite (Hawthorne *et al.* 2012) (Supplementary Fig. S2C). The predominant feature of Taranaki amphibole is the presence of breakdown textures such as reaction rims and volumetric decomposition, which are due to the effect of heating of amphibole to form anhydrous minerals of clinopyroxene, plagioclase and opaque minerals (D'Mello *et al.* 2021). Amphibole is generally absent from the groundmass. Oxides mainly occur as large inclusions in clinopyroxene crystals, glomerocrysts or dispersed in the groundmass and contribute up to *c.* 3 vol% to rock assemblages. They are mostly represented by titanomagnetite and rarely ilmenite, with occasional inclusions of sulfide. Rare olivine crystals are found in basaltic samples from Fanthams Peak, where amphibole is usually absent. Olivine crystals are anhedral and show thick reaction coronas of orthopyroxene. Few orthopyroxene grains are found in the groundmass. Additional BSE images of the samples are compiled in Supplementary Figure S3.

Discussion

The nature of the crystal cargo

Comparison of the crystal cargo of the lava samples with published mineral compositions from xenoliths (Gruender *et al.* 2010; Price *et al.* 2016) shows a virtually complete overlap, suggesting that the crystal cargo may be derived from deep crustal regions that also sourced the xenoliths (Fig. 4). Xenoliths found in Taranaki lavas are extremely diverse and include the following: (1) olivine-bearing ultramafic compositions (pyroxenite, troctolite, wehrlite and dunite); (2) cumulates or meta-igneous textured gabbros and diorites; (3) deep crustal mafic and felsic granulites and charnockites; (4) Cenozoic sediments from the Taranaki Basin (mudstone, siltstone, sandstone, greywacke and thermally metamorphosed sediments); (5) plutonic rocks (ultramafic to granitoid rocks including granodiorite, diorite and tonalite) from the Median Batholith, which is a remnant of an old magmatic arc (King and Thrasher 1996; Mortimer *et al.* 1997, 1999; Gruender *et al.* 2010; Price *et al.* 2011, 2016). According to Price *et al.* (2016), the isotopic compositions of the xenolith suite are consistent with the hypothesis that the xenoliths represent a complex sample of basement lithologies, cognate cumulates and/or crystal mushes and restitic material derived from partial melting of amphibolitic crust and material modified by metasomatic alteration associated with melts or fluids derived from both crustal and mantle sources.

It has been demonstrated that the crystal cargo of many arc magmas includes minerals that originate from disintegration of glomerocrysts, sometimes associated with the fragmentation of individual crystals (e.g. Zellmer *et al.* 2016). It has also been observed that some lavas are a product of crystal-poor magmas carrying phenocrysts from shallower regions (Shane *et al.* 2019). On observation, Taranaki rocks contain fractured phenocrysts with truncated zoning patterns (Fig. 3c and d). The majority of these crystals lack extensive rims, which would indicate that little or no crystallization took place after breaking. These observations and the compositional overlap of phenocrysts in the lavas with crystals from xenoliths (Fig. 4) point to a predominantly antecrystic or xenocrystic origin of the crystal cargo, apart from narrow overgrowth rims on clinopyroxene and plagioclase crystals. The microcrysts and microlites may be of autocrystic nature, although an antecrystic or xenocrystic origin cannot be precluded, as recently shown for microcrysts in andesites of the southern Taupo Volcanic Zone in New Zealand (Lormand *et al.* 2021).

To test for mineral–melt equilibrium, we distinguish crystal rims from mantles and cores because of the complex zoning histories observed in most crystals (Stewart *et al.* 1996; Price *et al.* 1999). For

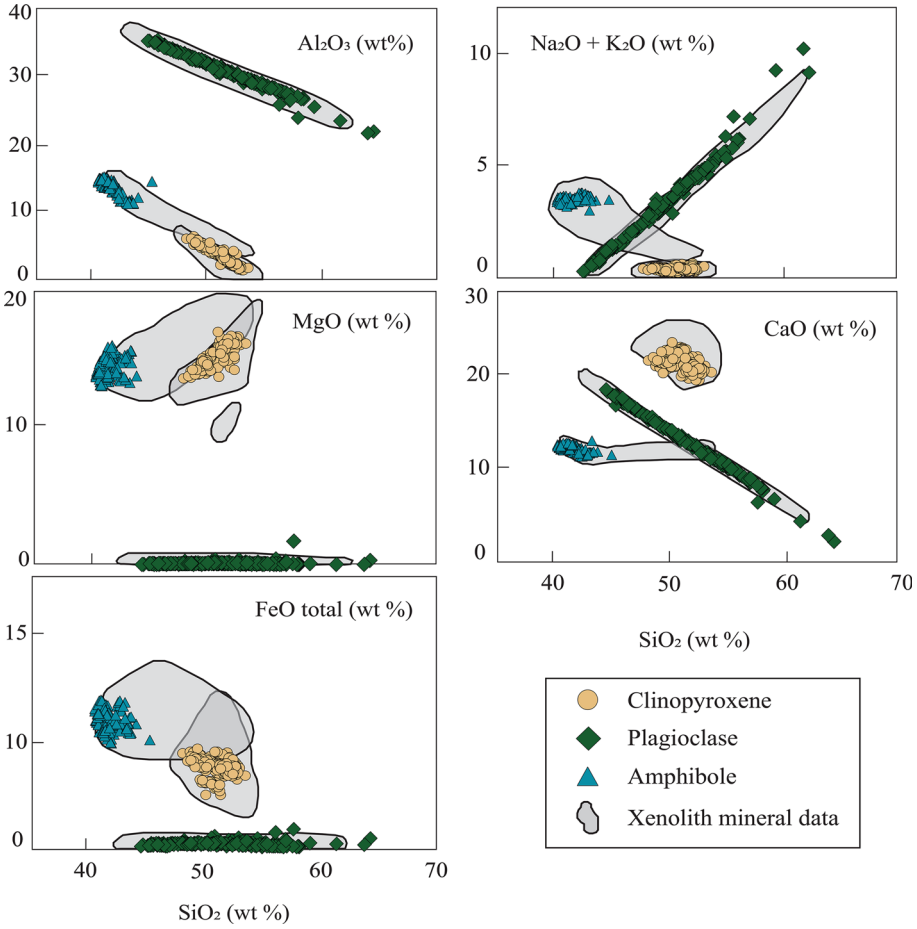

Fig. 4. Major element chemistry of mesocryst and macrocryst phases from Taranaki rocks (this work) compared with mineral data from xenoliths entrained in Taranaki lavas (Gruender *et al.* 2010; Price *et al.* 2016).

simplicity, and to account for potential misidentification of cores and mantles caused by sectional artefacts, we consider cores and mantles together. Groundmass major element compositions, which include microlite + glass, were used as the 'melt' composition for all thermometers, barometers and hygrometers.

Following Namur *et al.* (2012), plagioclase disequilibrium is demonstrated when the theoretically predicted anorthite content of plagioclase based on the given melt composition deviates from the measured An content of plagioclase (Fig. 5a). It is observed that plagioclase rims are generally in equilibrium, whereas the cores and mantles are more widely dispersed around the 1:1 line. A more robust equilibrium test uses the anorthite content of plagioclase versus the anorthite content of the melt (An_{liq}) based on equilibrium experiments of Waters and Lange (2015), and was first employed by Zellmer *et al.* (2016) (Fig. 5b). It is observed that the plagioclase compositions plot across the fields of water-oversaturated, -saturated and -undersaturated magma (as marked in Fig. 5b). Significant degrees of volatile oversaturation in magmas are implausible, and it is likely that the high-An cores and mantles were formed in equilibrium with a former melt of a much higher An content than the present carrier melt. The water-saturated rims are likely to have formed during ascent at very shallow depths ($\ll$200 MPa), where these magmas would saturate in H_2O irrespective of their original volatile contents. The presence of some water-undersaturated rims indicates that melts were not saturated at greater depth.

In clinopyroxene, chemical equilibrium between crystal rims and the melt is tested by comparing observed (measured) versus predicted (calculated) clinopyroxene components (DiHd, EnFs and CaTs) (Mollo *et al.* 2013) (Fig. 5c). This test for equilibrium was calibrated using Etnean basalts; however, the Fe–Mg (DiHd) equilibrium has also been applied to other alkaline systems (e.g. Putirka 2008; Ubide *et al.* 2014*a*, 2019). Most clinopyroxene rims plot close to the 1:1 line, whereas mantle and core compositions plot across a wider range, even if still within the equilibrium range. Although the clinopyroxenes satisfy conditions for chemical equilibrium, textural disequilibrium features such as reaction textures and resorption surfaces support disequilibrium for mantles and cores. Crystal rims appear to be in equilibrium with the melt.

Further evidence of disequilibrium is apparent in the formation of reaction textures on Taranaki amphiboles (see Supplementary Fig. S3), several of which are induced by heating rather than related to pre-eruptive decompression and degassing (D'Mello *et al.* 2021). We thus conclude that plagioclase and clinopyroxene rims are in equilibrium with the melt, whereas clinopyroxene and plagioclase mantles and cores, as well as amphibole crystals, are in disequilibrium.

Thermobarometry and hygrometry

Mineral–melt and mineral-only thermobarometers make it possible to estimate the crystallization conditions in magmatic systems (e.g. Putirka 2008). We combine groundmass with clinopyroxene rims, formed in equilibrium with the ascending melts and therefore indicators of silicate melt temperatures at the time of xenocryst or antecryst recycling and during the final stages of crystallization during ascent. On the other hand, owing to the predominance of disequilibrium textures and the absence of unreacted amphibole microlites in the groundmass, amphibole phenocrysts are considered recycled from crustal mushes, and are therefore useful thermometers for the intruded plutonic rocks or mushes sourcing the crystal cargo.

The clinopyroxene rim–melt thermometer of Petrelli *et al.* (2020) was used to estimate melt temperatures, whereas

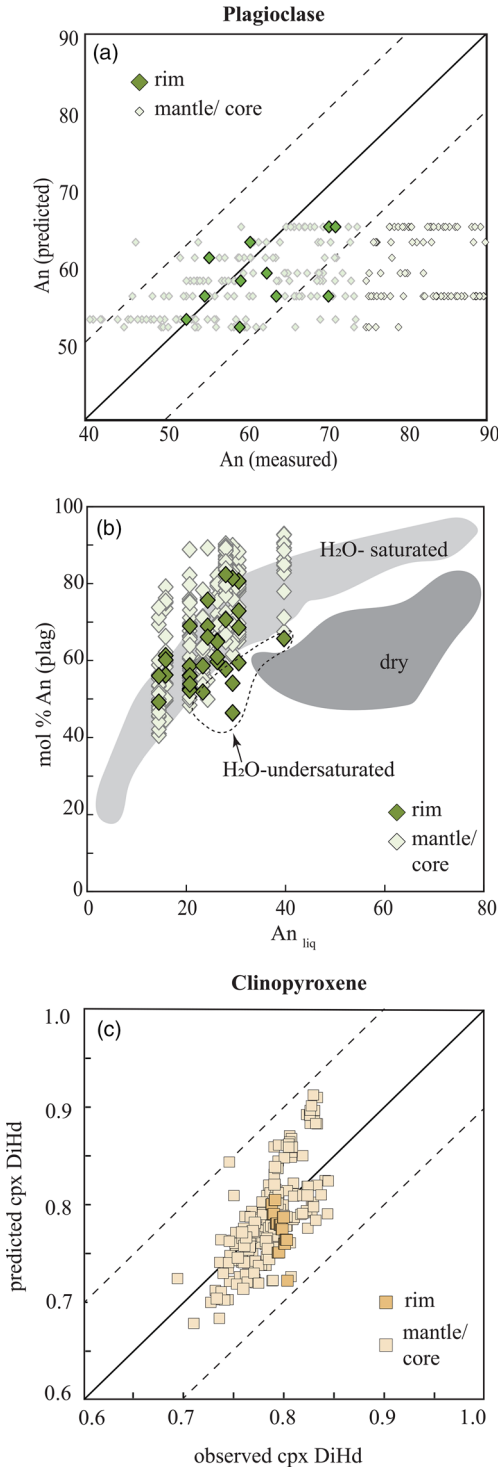

Fig. 5. Mineral–melt tests for equilibrium for plagioclase and clinopyroxene crystals from the investigated Taranaki rocks. Groundmass analyses are used as proxies for melt compositions. (**a**) Plagioclase–melt equilibrium after Namur *et al.* (2012). (**b**) Plagioclase–melt (groundmass) equilibrium after Zellmer *et al.* (2016); the light grey field represents data from water-saturated experiments, whereas the dark grey field represents data from dry experiments. (**c**) Clinopyroxene–melt equilibrium after Mollo *et al.* (2013), with dashed lines representing 1 SEE (standard error estimate) of the equilibrium condition.

amphibole-only thermobarometry of Ridolfi and Renzulli (2012) and Putirka (2016) was employed along with a clinopyroxene-only barometer (Petrelli *et al.* 2020) to estimate the temperature and pressure of the plutonic intrusions that sourced the crystal cargo. The thermobarometer of Petrelli *et al.* (2020) uses a machine learning approach employing a large range of compositions and is independent of the tectonic setting. The amphibole-only thermobarometer allows us to use amphibole compositions despite the presence of reaction rims, and the Ridolfi and Renzulli (2012) equations consider a large compositional range of amphiboles. Plagioclase rim–melt compositions were used to estimate silicate melt water contents using Waters and Lange (2015) and Putirka (2008) hygrometers, employing the Petrelli *et al.* (2020) thermometry results in the calculation.

Amphibole-only thermobarometry yields temperatures between 940 and 1010°C (±24°C), and pressure estimates between 300 and 600 MPa (±400 MPa) (Fig. 6). This corresponds well to the Group I, II and III xenoliths that show temperature ranges of 770–1010, 980–1050 and 860–1050°C respectively (Price *et al.* 2016). Clinopyroxene-only barometry returns consistent pressures that range from 200 to 600 MPa (±400 MPa) for mantles. However, the pressure estimates associated with both these barometers have very large uncertainties, essentially indicating that the crystals were formed somewhere within the Earth's crust (e.g. Wieser *et al.* 2022), and thus cannot be used for interpretations. Clinopyroxene rim–groundmass thermobarometry returns higher temperatures of 970–1100°C (±40°C) and lower pressures of 200–400 MPa (±200 MPa). Although the pressure estimates are imprecise, they point to shallow rim growth close to the surface, probably occurring at the onset of the eruption. Higher temperatures of melts relative to the ultrabasic to basic plutonic intrusions are evident in the comparison of clinopyroxene–melt and amphibole-only temperatures (see Fig. 6a).

Finally, the Waters and Lange (2015) and Putirka (2008) models yield low to moderate H_2O contents of Taranaki rocks that range from 1 to 3 wt% (±0.78 wt%) H_2O. Water contents show no correlation with the source vent (Fig. 6b).

Influence of antecrysts and xenocrysts on the whole-rock compositions

The influence of antecrysts on whole-rock compositions has been highlighted in porphyritic rocks from a range of settings (Larrea *et al.* 2013; Ubide *et al.* 2014*b*; Shane *et al.* 2019; Lormand *et al.* 2021). Taranaki magmas carry variable volume fractions of antecrysts and xenocrysts ranging from *c.* 35 to 55 vol% (Fig. 3g), and whole-rock compositions are significantly more SiO_2-poor than groundmass data (Fig. 2). However, whole-rock and groundmass datasets define separate sets of data where geochemical variability needs to be accounted for, with a direct correlation between crystal proportion and SiO_2 content not being observed. For example, in Figure 3g, the trachybasalt sample L16 shows a higher proportion of groundmass than the basaltic trachyandesite sample TUR. This indicates that there are additional factors that determine the whole-rock composition. The mineral chemistry of different lavas is similar, and their similar cargo suggests that chemical variations in carrier melts may play a significant role in the geochemical spread.

Based on the data obtained in this study, we propose that hot aphyric to sparsely phyric melts, ranging in composition from 55 to 68 wt % SiO_2 (groundmass data), have interacted with and remobilized crystals from the generally cooler rocks or melt-poor, low-silica mushes (940–1010°C based on amphibole geothermometry; Fig. 6a). Although the majority of crystals picked up are plagioclase, the entrainment of crystals still decreased the SiO_2 content of the originally hot, silica-rich melts by 5–11 wt%. This interaction triggers the formation of clinopyroxene rims at melt temperatures of around 970–1100°C (based on cpx rim–melt equilibrium). This model was tested using a simple mass-balance equation, $C_{wr} = XC_{min} + (1 - X)C_{melt}$, where C_{wr} is the whole-rock composition, C_{min} is the average mineral composition of the entrained crystal cargo, with average mineral analyses of each phase

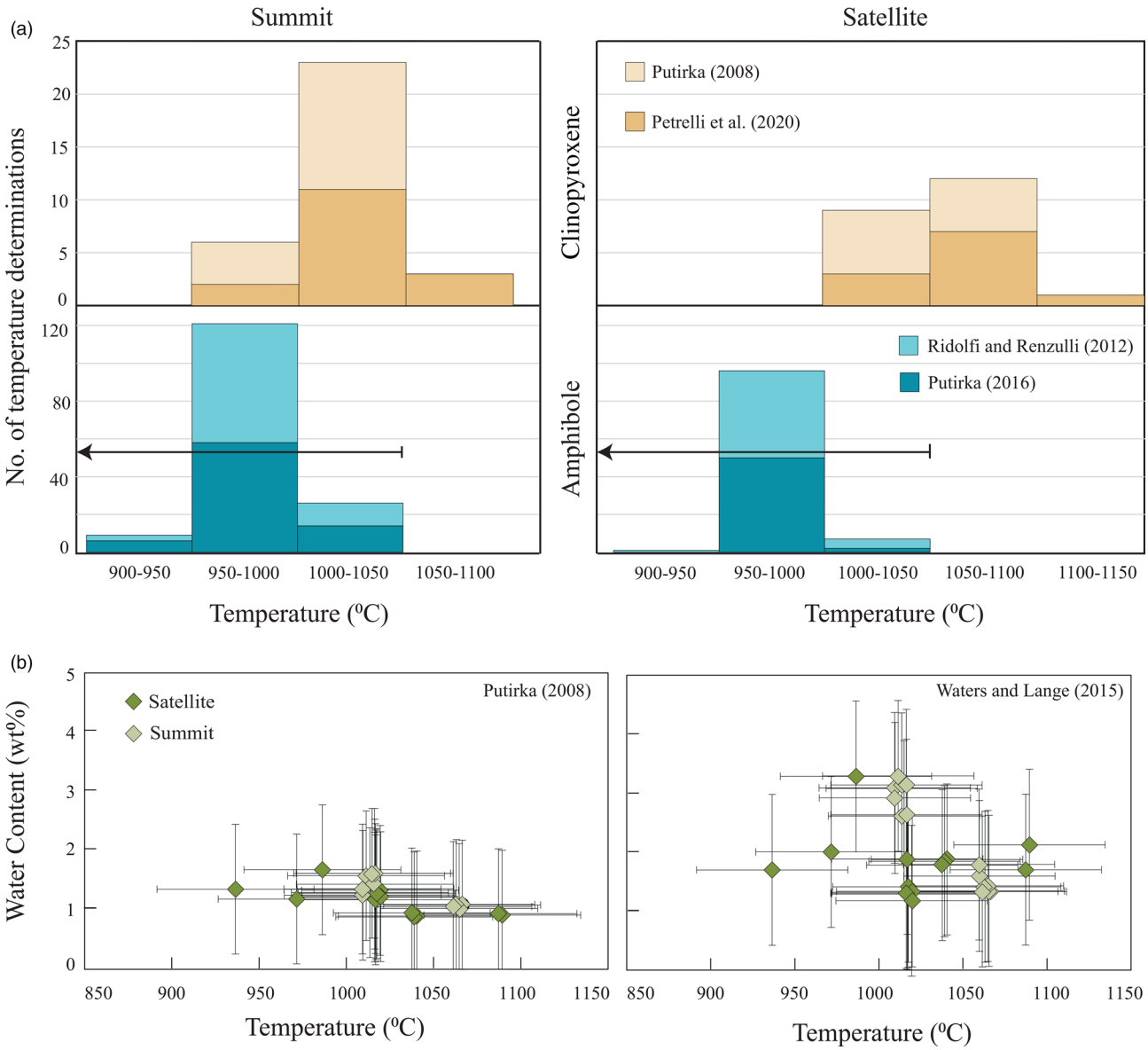

Fig. 6. (**a**) Frequency histograms showing the results of clinopyroxene–melt and amphibole-only geothermometric calculations (Putirka 2008, 2016; Ridolfi and Renzulli 2012; Petrelli *et al.* 2020) for the investigated summit and satellite Taranaki rocks. We compare temperatures from clinopyroxene–melt thermometry and amphibole-only thermometry for the summit and satellite eruptive rocks. (**b**) Results of the plagioclase–melt hygrometers by Waters and Lange (2015) and Putirka (2008) v. temperature estimates obtained from the clinopyroxene–melt geothermometer by Petrelli *et al.* (2020) for the investigated summit and satellite Taranaki rocks. The uncertainty in water content of ±0.35 wt% from the model by Waters and Lange (2015) is combined here with the estimated temperature uncertainty of ±40°C (Petrelli *et al.* 2020) to yield a total uncertainty of *c.* ±0.78 wt%, whereas the uncertainty on the Putirka (2008) hygrometer is *c.* 1.1 wt%. In both diagrams, groundmass analyses are used as proxies for melt compositions.

for each of the investigated samples (amp + cpx + pl), C_{melt} is the groundmass composition and X is the mineral proportion (as obtained from modal analysis). Based on this equation, we predict whole-rock compositions and compare them with the measured data (see Supplementary Fig. S4). Predicted versus observed compositions plot in close proximity to the 1:1 line for the major oxides, Al_2O_3, CaO, Na_2O and K_2O. Whole-rock predictions are somewhat below natural data for SiO_2 and higher for TiO_2, FeO and MgO. Petrographic observations show that plagioclase is a dominant phase of macrocrysts and mesocrysts. Microcryst populations, however, contain significantly higher amounts of mafic mineral phases, such as titanomagnetite, clinopyroxene, orthopyroxene and olivine. As our mass balance did not consider microcrysts <80 μm in length, the difference in measured and predicted values of whole-rock compositions can be attributed to such microcrysts of mafic minerals, which are not accounted for in measured groundmass or mineral phase analyses.

Generation of intermediate to acid parental melts at Mt Taranaki

The generation of variable magma compositions at Taranaki has been attributed to fractional crystallization of parental basalts and assimilation of continental crust in a deep crustal hot zone (DCHZ) following mixing, assimilation, storage and hybridization (MASH) processes (Stewart *et al.* 1996; Price *et al.* 1999, 2016; Zernack *et al.* 2012). We tested this hypothesis by comparing our data with hydrous (Melekhova *et al.* 2013; Nandedkar *et al.* 2014) crystallization experiments conducted at pressures relevant to the deep crust. Figure 7 shows a comparison of temperature and SiO_2 content of a typical DCHZ melt suite, together with melt thermometric constraints from Taranaki samples. Taranaki melt temperatures, determined by cpx rim–groundmass geothermometry, are significantly higher than DCHZ experimental melts. If basaltic mantle melts resided in a DCHZ and differentiated towards

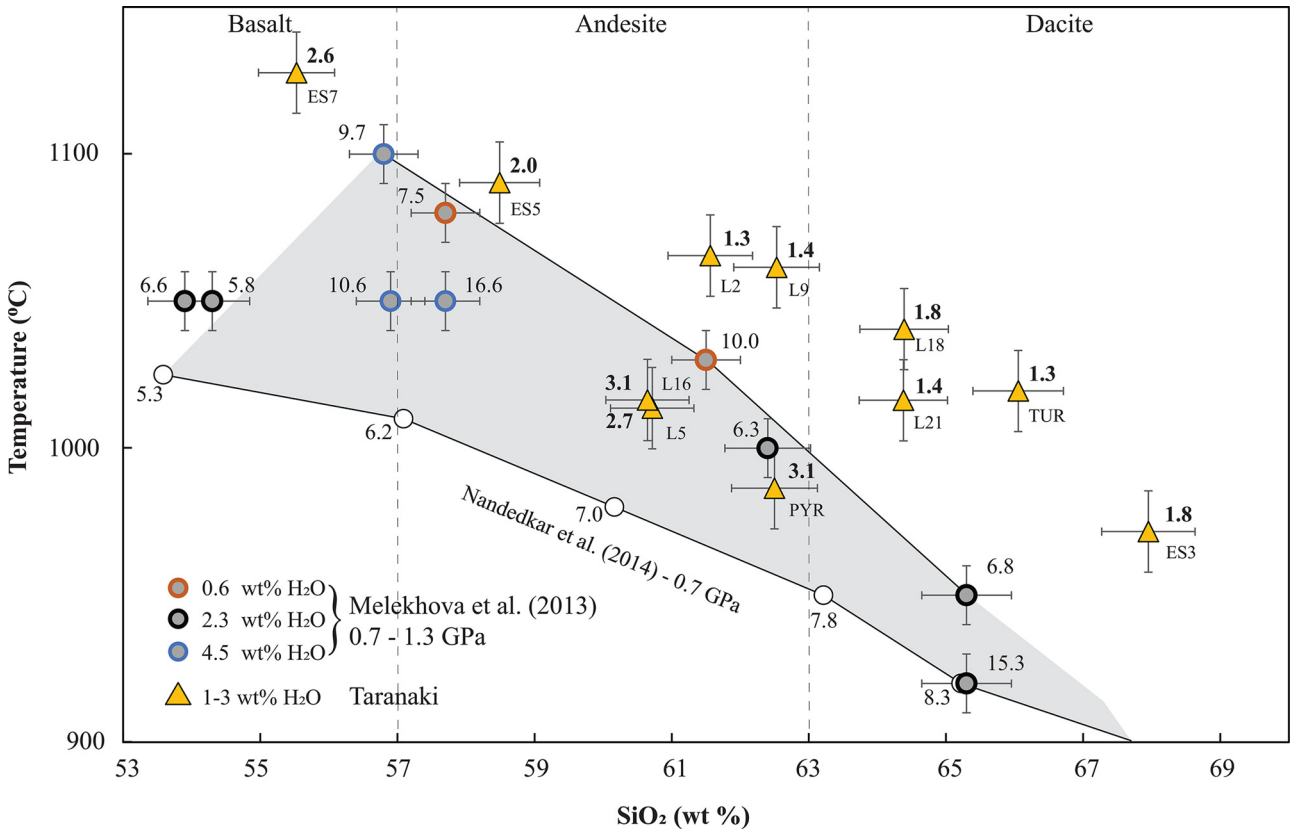

Fig. 7. Silica–temperature relationship of Taranaki rocks groundmasses, together with water-saturated (Nandedkar *et al.* 2014) and variably hydrous (starting water contents of 0.6, 2.3 and 4.5 wt%) (Melekhova *et al.* 2013) experimental magmas simulating a deep crustal hot zone. Numbers by the circles show the water contents of experimental run products (in wt%), bold values the water content for the given sample. Water contents are based on the hygrometer of Waters and Lange (2015) and temperatures on the clinopyroxene–melt thermometer of Petrelli *et al.* (2020).

more silicic compositions at Taranaki, the temperatures recorded would be lower at any given SiO_2 content. Experiments conducted by Melekhova *et al.* (2013) also suggest that the DCHZ magmas become hydrous at depth and therefore would reach water saturation during ascent, prior to reaching the upper crust. The preservation of some plagioclase rims indicating H_2O undersaturation (Fig. 4b) suggests that H_2O saturation was not achieved at depth for these samples, corroborating our notion that DCHZ differentiation may not be a feasible petrogenetic scenario at Taranaki volcano in Holocene times.

The melts of Taranaki are thus paradoxical: they show temperatures typical of mantle-generated melts but also have trace element ratios, Mg# and Ni and Cr concentrations typical of magmas modified through the input of crustal material. Indeed, La/Yb ratios for Taranaki range from 5.91 to 10.64, La/Sm from 3.72 to 4.61 and Mg# is <40, Ni is <22 ppm and Cr is <50 ppm (except for samples TUR and ES5 where Cr is between 120 and 150 ppm). This can be explained by invoking the subduction mélange model.

During subduction of an oceanic plate beneath a continental plate (as in the case of New Zealand) material from the overriding plate is eroded along with the altered oceanic crust (AOC) and hydrous ultramafic matrix that originates from the mantle wedge or the incoming oceanic lithosphere. Subduction mélanges are solid-state mixtures of this AOC, forearc crust (FAC) debris and ultramafic matrices (Marschall and Schumacher 2012; Parolari *et al.* 2021). The mixing of mélange components occurs initially in the forearc and then in the mantle, where partial melting of these components can yield diverse melts with little to no contribution from the mantle. Mélanges have a lower solidus and density than the surrounding mantle and can thus rise spontaneously into the core of the wedge, where they will melt (Gerya and Yuen 2003; Behn *et al.* 2011). This can account for diverse felsic melts at mantle depths with crustal assimilation-like chemistry of high K_2O, SiO_2, La/Sm and La/Yb. The simple mixing of eroded forearc material and AOC with sediments to form the mélange melt source was demonstrated elsewhere, such as the Trans-Mexican Volcanic Belt (Parolari *et al.* 2021).

In line with this alternative model, we consider the trace element, specifically Nd, Hf and Sr, and isotopic compositions ($^{87}Sr/^{86}Sr$ and $^{143}Nd/^{144}Nd$) of Taranaki whole-rock and xenolith samples, which are available for Taranaki eruptive rocks (Stewart *et al.* 1996; Price *et al.* 1999, 2016). As evident from Figure 8, the bulk of the xenoliths overlap with whole-rock compositions in trace element and isotopic space (Fig. 8). If the crystal cargo of Taranaki samples is indeed representing the disintegration of xenoliths as suggested from Figure 4, whole-rock compositions will be very similar to the groundmass compositions, largely reflecting the Taranaki melt prior to entrainment of plutonic crystal cargo.

The conventional model of subduction melt generation suggests that AOC-derived fluids and sediment partial melts react with the overlying mantle to produce basaltic melts. However, the arc lavas typically show much lower Nd/Sr ratios than expected from bulk mixing of slab components (AOC, FAC and sediment) with sediment partial melts as low as 1%, and would be represented as a convex line in Figure 8a (see Nielsen and Marschall 2017). In contrast, bulk mixing of crustal components and depleted mantle more closely approximates arc volcanic rocks (Nielsen and Marschall 2017). Can this alternative model also apply in the case of back-arc volcanism? We see that Taranaki lava samples plot along similar trends to those for other arc lavas for which the subduction mélange model has been invoked (Fig. 8a). To produce the isotopic ratios of Taranaki rocks, mixing between a large

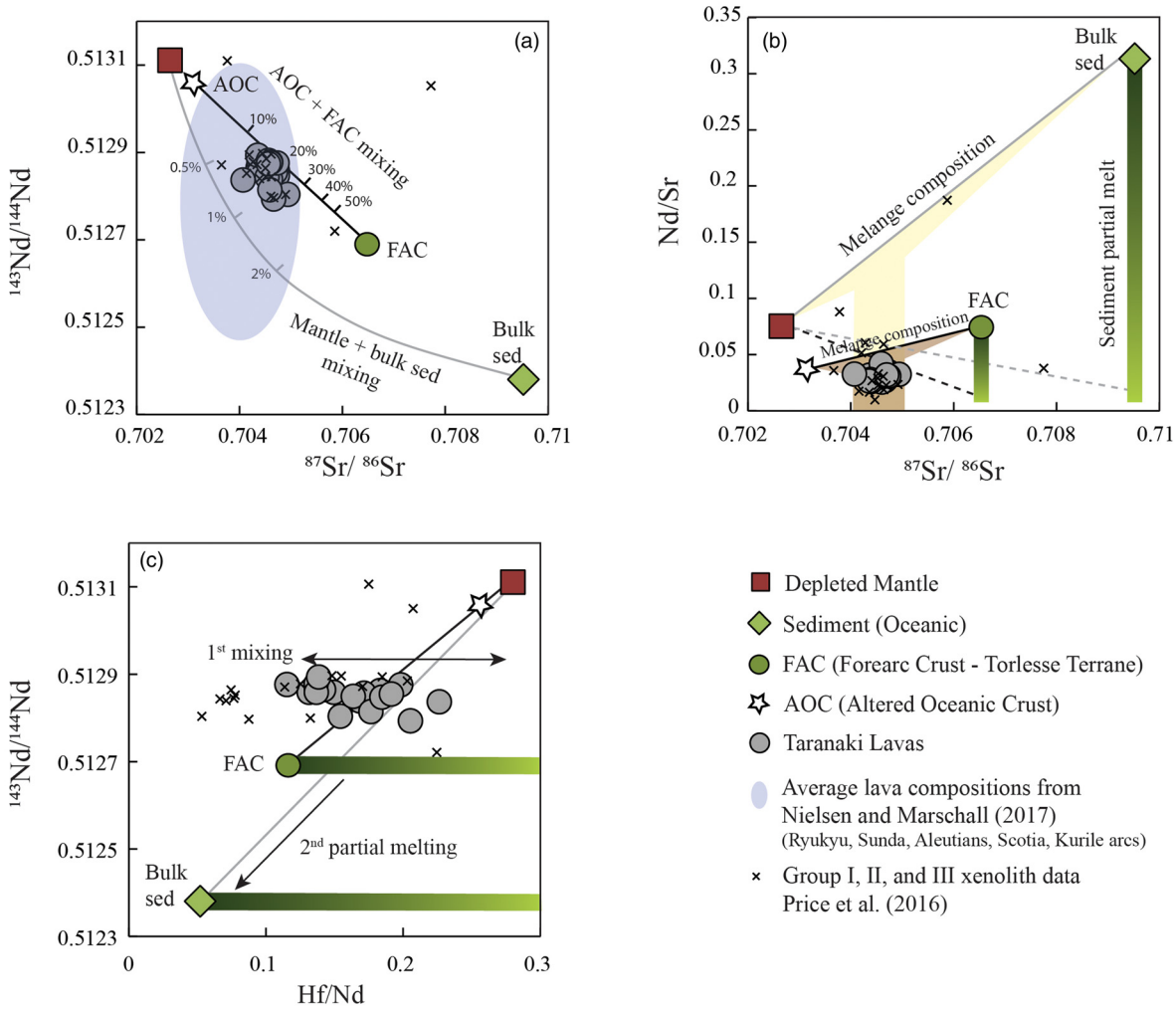

Fig. 8. Trace element and isotopic ratios for Taranaki whole-rock (Stewart *et al.* 1996) and xenolith data (Price *et al.* 2016), plotted on petrogenetic model diagrams by Nielsen and Marschall (2017) for comparison. The model for Taranaki rocks uses Pacific sediments (Plank *et al.* 2013), subducting slab for New Zealand altered oceanic crust (AOC; Castillo *et al.* 2009; Turner *et al.* 2009*b*), Taranaki lavas (Price *et al.* 1992) and forearc crust (FAC; Torlesse Terrane averages) (Price *et al.* 2015) and depleted mantle (Salters and Stracke 2004). (**a**) $^{87}Sr/^{86}Sr$ v. $^{143}Nd/^{144}Nd$ with bold line tracing mixing of AOC and FAC, whereas grey line shows mixing between depleted mantle and bulk sediment. Blue field shows composition of global arc magmas. (**b**) Nd/Sr v. $^{87}Sr/^{86}Sr$ showing mixing between depleted mantle and oceanic sediments or sediment partial melts and bulk sediment mixing to form a mélange (yellow field). Also represented is the mélange (brown field) formed through the mixing of AOC with FAC or FAC partial melts. Vertical green bars show mixing lines between depleted mantle with 1% sediment–FAC melt (fine dashed line) to bulk mixing or complete melting of sediment–FAC (bold dashed line). (**c**) $^{143}Nd/^{144}Nd$ v. Hf/Nd showing mixing lines between mantle and bulk sediment–FAC. Horizontal bars indicate the range of melt compositions possible for sediment–FAC melting down to 1%.

proportion of mantle material with <2% subducted sediments is required. However, high mantle proportions cannot produce lavas with low Mg# and Cr and Ni contents and a strong crustal signature, which are typical of Taranaki's Holocene activity. These isotopic signatures, however, can be produced through the mixing of eroded forearc crust with AOC, followed by their partial melting (Fig. 8b). Taranaki $^{87}Sr/^{86}Sr$ v. Nd/Sr ratios show that mélange compositions with *c.* 20% FAC mixing with AOC would produce the compositions observed upon partial melting of the mélange (dark brown field). Although similar compositions are possible through the partial melting of a depleted mantle and bulk sediment mélange (yellow field), the $^{87}Sr/^{86}Sr$ v. $^{143}Nd/^{144}Nd$ ratios (Fig. 8a) do not conform to this interpretation. The narrow range of isotopic ratios further indicates the limited role of slab fluids and partial melting of the depleted mantle in the generation of Taranaki magmas. The spread of Hf/Nd values (Fig. 8c) at relatively constant $^{143}Nd/^{144}Nd$ (as well as $^{87}Sr/^{86}Sr$) indicates that mixing is the predominant process that occurs before melting, because if melting had preceded mixing the isotopic data would show a wider spread of values. However, to better quantify the relative proportions of subducted forearc crust, altered oceanic crust and sediment components involved in intermediate to acid melt generation at Taranaki, future work should consider the specific isotopic compositions of such components and of the groundmass of volcanic products.

Our data suggest that the subducted Hikurangi plate, SE of Taranaki, may release a subduction mélange diapir into the peridotitic mantle wedge (Fig. 9). This mélange is composed of various components including the eroded FAC, AOC and possibly some sediment, and they mix in varying proportions (Fig. 8a). The mélange diapirs and their principal elements have been illustrated by Marschall and Schumacher (2012). The interface between the mantle and the diapir can undergo partial melting owing to decompression, heating and influx of fluid. These diapirs can also rise through the mantle wedge with minimal interaction with the mantle (e.g. Straub *et al.* 2011; Parolari *et al.* 2021). Depending on the contribution of the mélange components and the region from which the melt is tapped, the composition of the melt would vary. Higher forearc crustal input and melts from the central region of the mélange would result in intermediate–acid compositions, whereas melts tapped from the edges of the mélange with more AOC and

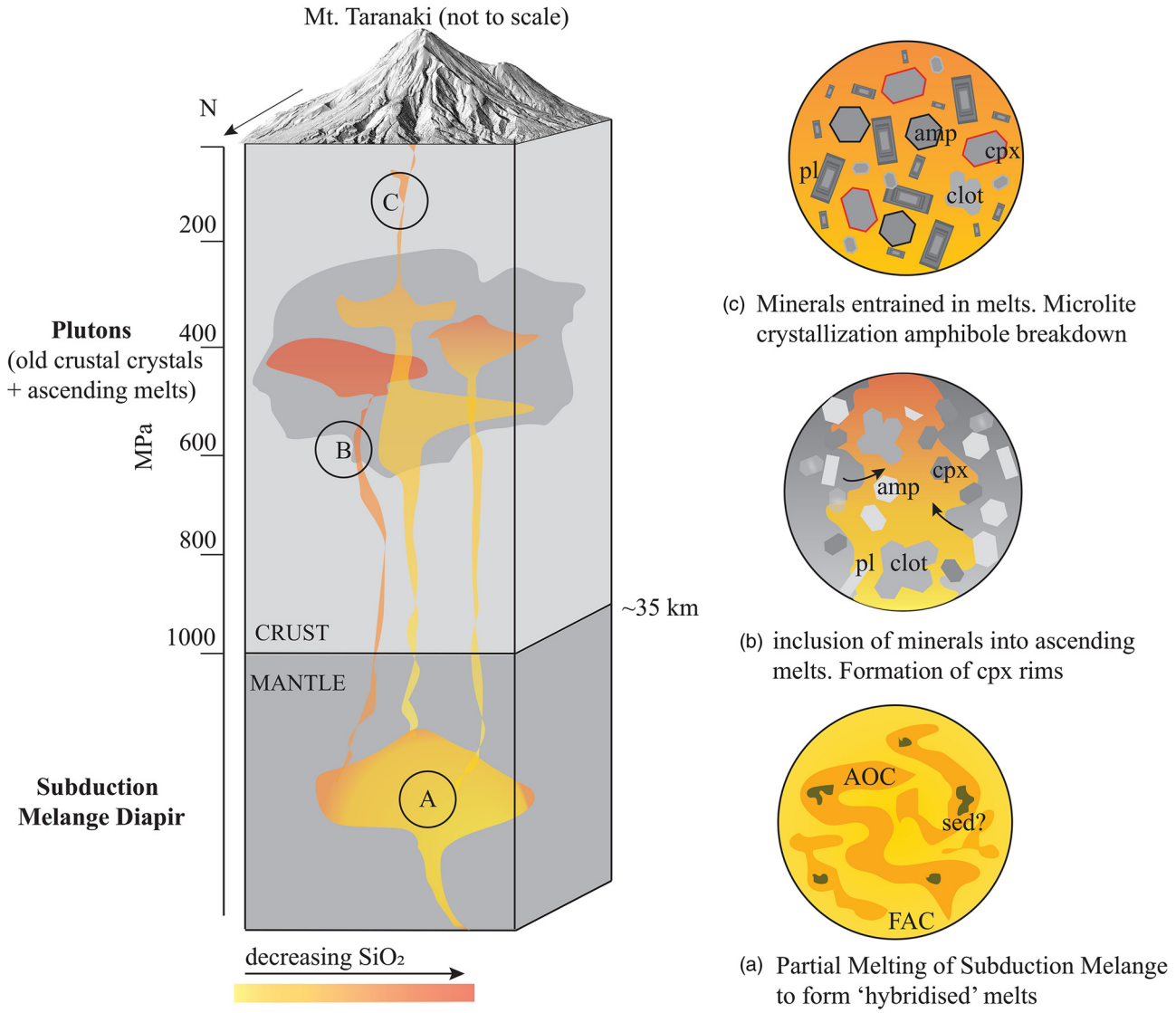

Fig. 9. Schematic diagram showing proposed melt generation and evolution in Taranaki. Subduction mélange diapirs rise from the Hikurangi Plate and interact with the mantle wedge beneath Taranaki heterogeneously to produce melts of variable compositions based on the relative contribution of each component. (**a**) These diverse melts then rise through the crust and interact with mafic plutonic rocks of the basement and/or with crystal-rich mushes, remobilizing and entraining crystals from these. As a result, magma compositions (melts + recycled crystals) are reduced in silica. (**b**) Ascent of the magmas through the shallow crust and through the edifice results in plagioclase, clinopyroxene and oxide microlite crystallization, formation of plagioclase and clinopyroxene rims in equilibrium with the melt, and breakdown of hydrous amphibole (**c**).

mantle input would have basic–intermediate compositions owing to the contribution of the depleted mantle. Subcrustal mixing of end-member acid and basic melts results in a range of intermediate compositions with high temperatures typical of the wedge core (up to *c.* 1300°C) (England and Katz 2010). These melts then rise from the mantle into the crust, initially forming few, if any, crystals. As melt batches ascend, they encounter the relatively cold, mafic plutonic rocks that currently form the basement of Taranaki. Considering the history of Mt Taranaki spans over 200 kyr, repeated injections of magma may have resulted in the formation of a crystal-rich mush system with minerals disintegrating from older plutons and those crystallizing from older ponded melts. Most magmas (mélange melt + remobilized crystals) probably fail to ascend to the surface, but instead form intrusions that may rapidly solidify to yield plutons. Those magmas that breach the surface carry remobilized crystals from the plutonic rocks or melt-poor mushes, with new rims formed in equilibrium with the intermediate to acid host melt, with the exception of amphiboles, most of which show breakdown textures and are not present in the groundmass (D'Mello *et al.* 2021). Thus, even in the case of a back-arc volcano such as Taranaki, subduction dynamics may conserve and recycle crustal material from the eroded forearc, in the case presented here with limited mantle contribution (Straub *et al.* 2011; Parolari *et al.* 2021). However, future studies that consider melt isotopic data as opposed to whole-rock data will be required to better quantify the relative contributions of these components, and to assess if there have been any changes in petrogenetic processes over the lifetime of this back-arc volcano.

Conclusions

(1) Mineral–melt chemical disequilibrium and the compositional overlap between phenocrysts in Taranaki lava samples and mineral data from xenoliths indicate that recycled antecrysts and xenocrysts are the prevalent components of the macro- and mesocryst populations in Taranaki rocks.

(2) Thermobarometry suggests that hot, intermediate–acid melts intruded into colder, plutonic rocks and/or crystal-poor mushes, remobilizing and entraining crystals. The

melts were moderately hydrous (although not all reach H_2O-saturation at depth) and contained few (if any) crystals before interacting with the plutons or mushes.

(3) The presence and proportion of antecrysts and xenocrysts strongly influence the range of whole-rock compositions observed at Mt Taranaki, and probably globally at other arc volcanoes. However, groundmass compositional variations across our sample set also require other petrogenetic processes to control the geochemical diversity of erupted magmas.

(4) We suggest that hot, intermediate–acid parental melts differentiate to lower silica bulk compositions through the uptake of plagioclase + clinopyroxene + amphibole crystal cargoes. This is in contrast to classic crustal differentiation models of basaltic mantle melts following MASH processes in a deep crustal hot zone. Our data from recent Taranaki rocks agree with ascent of hot, aphyric to sparsely phyric and occasionally H_2O-undersaturated intermediate composition parental melts, generated by partial melting of subduction mélange diapirs for the youngest flows of Taranaki.

Scientific editing by Lorenzo Fedele

Acknowledgements We thank R. Brahm, D. Coulthard Jr, T. Hancock, M. Rowe and C. Corella Santa Cruz for providing feedback on the paper and fieldwork assistance. We also thank A. Moebis, J. Caulfield and M. McAteer for their assistance in the laboratory. Reviews by B. Ellis and three anonymous reviewers and the editorial comments of L. Fedele improved this paper significantly.

Author contributions **NGD**: conceptualization (lead), data curation (lead), formal analysis (lead), investigation (lead), methodology (equal), writing – original draft (lead); **GFZ**: conceptualization (equal), funding acquisition (lead), methodology (supporting), supervision (lead), visualization (supporting), writing – review & editing (equal); **GK**: data curation (supporting), software (supporting), supervision (supporting), writing – review & editing (supporting); **TU**: data curation (supporting), formal analysis (supporting), methodology (supporting), writing – review & editing (supporting); **JNP**: funding acquisition (lead), resources (supporting), supervision (supporting), writing – review & editing (supporting); **RBS**: data curation (supporting), writing – review & editing (supporting)

Funding This work was funded by the Massey University, Massey Foundation and Royal Society Te Apārangi.

Competing interests The authors declare that they have no known competing financial interests or personal relationships that could have appeared to influence the work reported in this paper.

Data availability All data generated or analysed during this study are included in this published article and its supplementary information files.

Correction notice The copyright has been updated to Open Access.

References

Annen, C., Blundy, J.D. and Sparks, R.S.J. 2006. The genesis of intermediate and silicic magmas in deep crustal hot zones. *Journal of Petrology*, **47**, 505–539, https://doi.org/10.1093/petrology/egi084

Ballance, P.F. 1976. Evolution of the Upper Cenozoic Magmatic Arc and plate boundary in northern New Zealand. *Earth and Planetary Science Letters*, **28**, 356–370, https://doi.org/10.1016/0012-821X(76)90197-7

Behn, M.D., Kelemen, P.B., Hirth, G., Hacker, B.R. and Massonne, H.-J. 2011. Diapirs as the source of the sediment signature in arc lavas. *Nature Geoscience*, **4**, 641–646, https://doi.org/10.1038/ngeo1214

Boddington, T., Parkin, C.J. and Gubbins, D. 2004. Isolated deep earthquakes beneath the North Island of New Zealand. *Geophysical Journal International*, **158**, 972–982, https://doi.org/10.1111/j.1365-246X.2004.02340.x

Cashman, K.V. and McConnell, S.M. 2005. Multiple levels of magma storage during the 1980 summer eruptions of Mount St. Helens, WA. *Bulletin of Volcanology*, **68**, 57–75, https://doi.org/10.1007/s00445-005-0422-x

Castillo, P.R., Lonsdale, P.F., Moran, C.L. and Hawkins, J.W. 2009. Geochemistry of mid-Cretaceous Pacific crust being subducted along the Tonga–Kermadec Trench: implications for the generation of arc lavas. *Lithos*, **112**, 87–102, https://doi.org/10.1016/j.lithos.2009.03.041

Cronin, S.J., Zernack, A.V. *et al.* 2021. The geological history and hazards of a long-lived stratovolcano, Mt. Taranaki, New Zealand. *New Zealand Journal of Geology and Geophysics*, **64**, 456–478, https://doi.org/10.1080/00288306.2021.1895231

Damaschcke, M., Cronin, S.J., Holt, K.A., Bebbington, M.S. and Hogg, A.G. 2017. A 30 000 yr high-precision eruption history for the andesitic Mt. Taranaki, North Island, New Zealand. *Quaternary Research*, **87**, 1–23, https://doi.org/10.1017/qua.2016.11

Davidson, J.P., Hora, J.M., Garrison, J.M. and Dungan, M.A. 2005. Crustal forensics in arc magmas. *Journal of Volcanology and Geothermal Research*, **140**, 157–170, https://doi.org/10.1016/j.jvolgeores.2004.07.019

Dimech, J.-L., Stern, T. and Lamb, S.J.G. 2017. Mantle earthquakes, crustal structure, and gravitational instability beneath western North Island, New Zealand. *Geology*, **45**, 155–158, https://doi.org/10.1130/G38476.1

D'Mello, N.G., Zellmer, G.F. *et al.* 2021. Deciphering magma storage and ascent processes of Taranaki, New Zealand, from the complexity of amphibole breakdown textures. *Lithos*, **398–399**, 106264, https://doi.org/10.1016/j.lithos.2021.106264

England, P.C. and Katz, R.F. 2010. Melting above the anhydrous solidus controls the location of volcanic arcs. *Nature*, **467**, 700–703, https://doi.org/10.1038/nature09417

Gerya, T.V. and Yuen, D.A. 2003. Rayleigh–Taylor instabilities from hydration and melting propel 'cold plumes' at subduction zones. *Earth and Planetary Science Letters*, **212**, 47–62, https://doi.org/10.1016/S0012-821X(03)00265-6

Giba, M., Nicol, A. and Walsh, J.J. 2010. Evolution of faulting and volcanism in a back-arc basin and its implications for subduction processes. *Tectonics*, **29**, https://doi.org/10.1029/2009TC002634

Gill, J.B. 1981. *Orogenic Andesites and Plate Tectonics*. Springer, Berlin.

Grove, T.L. and Donnelly-Nolan, J.M. 1986. The evolution of young silicic lavas at Medicine Lake Volcano, California: implications for the origin of compositional gaps in calc-alkaline series lavas. *Contributions to Mineralogy and Petrology*, **92**, 281–302, https://doi.org/10.1007/BF00572157

Gruender, K., Stewart, R.B. and Foley, S. 2010. Xenoliths from the sub-volcanic lithosphere of Mt Taranaki, New Zealand. *Journal of Volcanology and Geothermal Research*, **190**, 192–202, https://doi.org/10.1016/j.jvolgeores.2009.09.014

Hawthorne, F.C., Oberti, R., Harlow, G.E., Maresch, W.V., Martin, R.F., Schumacher, J.C. and Welch, M.D. 2012. Nomenclature of the amphibole supergroup. *American Mineralogist*, **97**, 2031–2048, https://doi.org/10.2138/am.2012.4276

Hildreth, W. and Moorbath, S. 1988. Crustal contributions to arc magmatism in the Andes of Central Chile. *Contributions to Mineralogy and Petrology*, **98**, 455–489, https://doi.org/10.1007/BF00372365

Iddings, J.P. 1892. On the crystallization of igneous rocks. *Bulletin of the Philosophical Society of Washington*, **11**, 71–112.

Jarosewich, E., Nelen, J.A. and Norberg, J.A. 1980. Reference samples for electron microprobe analysis. *Geostandards Newsletter*, **4**, 43–47, https://doi.org/10.1111/j.1751-908X.1980.tb00273.x

King, P.R. and Thrasher, G.P. 1996. *Cretaceous-Cenozoic geology and petroleum systems of the Taranaki Basin, New Zealand*. Institute of Geological & Nuclear Sciences Monograph, **13**, Institute of Geological & Nuclear Sciences.

Larrea, P., França, Z., Lago, M., Widom, E., Galé, C. and Ubide, T.J.J.O.P. 2013. Magmatic processes and the role of antecrysts in the genesis of Corvo Island (Azores Archipelago, Portugal). *Journal of Petrology*, **54**, 769–793, https://doi.org/10.1093/petrology/egs084

Le Maître, R.W. 2002. *Igneous Rocks: A Classification and Glossary of Terms. Recommendations of the International Union of Geological Sciences, Sub-Commission on the Systematics of Igneous Rocks*. Cambridge University Press.

Lerner, G.A., Cronin, S.J., Turner, G.M. and Rowe, M.C. 2019. Paleomagnetic determination of the age and properties of the 1780–1800 AD dome effusion/collapse episode of Mt. Taranaki, New Zealand. *Bulletin of Volcanology*, **81**, 15, https://doi.org/10.1007/s00445-019-1275-z

Locke, C.A., Cassidy, J. and MacDonald, A. 1994. Constraints on the evolution of the Taranaki volcanoes, New Zealand, based on aeromagnetic data. *Bulletin of Volcanology*, **56**, 552–560, https://doi.org/10.1007/BF00302835

Lormand, C., Zellmer, G.F. *et al.* 2021. Shallow magmatic processes revealed by cryptic microantecrysts: a case study from the Taupo Volcanic Zone. *Contributions to Mineralogy and Petrology*, **176**, 97, https://doi.org/10.1007/s00410-021-01857-7

Marschall, H.R. and Schumacher, J.C. 2012. Arc magmas sourced from mélange diapirs in subduction zones. *Nature Geoscience*, **5**, 862, https://doi.org/10.1038/ngeo1634

Melekhova, E., Annen, C. and Blundy, J. 2013. Compositional gaps in igneous rock suites controlled by magma system heat and water content. *Nature Geoscience*, **6**, 385–390, https://doi.org/10.1038/ngeo1781

Melekhova, E., Blundy, J., Robertson, R. and Humphreys, M.C.S. 2014. Experimental evidence for polybaric differentiation of primitive arc basalt beneath St. Vincent, Lesser Antilles. *Journal of Petrology*, **56**, 161–192, https://doi.org/10.1093/petrology/egu074

Mollo, S., Putirka, K., Misiti, V., Soligo, M. and Scarlato, P. 2013. A new test for equilibrium based on clinopyroxene–melt pairs: clues on the solidification temperatures of Etnean alkaline melts at post-eruptive conditions. *Chemical Geology*, **352**, 92–100, https://doi.org/10.1016/j.chemgeo.2013.05.026

Morimoto, N. 1988. Nomenclature of Pyroxenes. *Mineralogy and Petrology*, **39**, 55–76, https://doi.org/10.1007/BF01226262

Mortimer, N., Tulloch, A.J. and Ireland, T.R. 1997. Basement geology of Taranaki and Wanganui Basins, New Zealand. *New Zealand Journal of Geology and Geophysics*, **40**, 223–236, https://doi.org/10.1080/00288306.1997.9514754

Mortimer, N., Gans, P., Calvert, A. and Walker, N. 1999. Geology and thermochronometry of the east edge of the Median Batholith (Median Tectonic Zone): a new perspective on Permian to Cretaceous crustal growth of New Zealand. *Island Arc*, **8**, 404–425, https://doi.org/10.1046/j.1440-1738.1999.00249.x

Namur, O., Charlier, B., Toplis, M.J. and Vander Auwera, J. 2012. Prediction of plagioclase–melt equilibria in anhydrous silicate melts at 1-atm. *Contributions to Mineralogy and Petrology*, **163**, 133–150, https://doi.org/10.1007/s00410-011-0662-z

Nandedkar, R.H., Ulmer, P. and Müntener, O. 2014. Fractional crystallization of primitive, hydrous arc magmas: an experimental study at 0.7 GPa. *Contributions to Mineralogy and Petrology*, **167**, 1–27, https://doi.org/10.1007/s00410-014-1015-5

Neall, V.E. 1979. *Sheets P19, P20, and P21. New Plymouth, Egmont and Manaia. Geological map of New Zealand 1:50 000*, 1st edn. New Zealand Geological Survey.

Neall, V.E., Stewart, R.B. and Smith, I.E.M. 1986. History and petrology of the Taranaki volcanoes. *In*: Smith, I.E.M. (ed.) *Late Cenozoic Volcanism in New Zealand*. Royal Society New Zealand Bulletin, **23**, 251–263.

Nielsen, S.G. and Marschall, H.R. 2017. Geochemical evidence for mélange melting in global arcs. *Science Advances*, **3**, e160240, https://doi.org/10.1126/sciadv.1602402

Palme, H. and O'Neill, H.S.C. 2003. Cosmochemical estimates of mantle composition. *In*: Carlson, C.W. (ed.) *The Mantle and Core*. Treatise on Geochemistry, **2**, Elsevier 568.

Parolari, M., Gómez-Tuena, A., Errázuriz-Henao, C. and Cavazos-Tovar, J.G. 2021. Orogenic andesites and their link to the continental rock cycle. *Lithos*, **382**, 105958, https://doi.org/10.1016/j.lithos.2020.105958

Petrelli, M., Caricchi, L. and Perugini, D. 2020. Machine learning thermobarometry: application to clinopyroxene-bearing magmas. *Journal of Geophysical Research: Solid Earth*, **125**, e2020JB020130, https://doi.org/10.1029/2020JB020130

Platz, T. 2007. *Understanding aspects of andesitic dome-forming eruptions through the last 1000 yrs of volcanism at Mt. Taranaki, New Zealand*. Doctoral dissertation, Massey University.

Platz, T., Cronin, S.J., Cashman, K.V., Stewart, R.B. and Smith, I.E.M. 2006. Transition from effusive to explosive phases in andesite eruptions – a case-study from the AD1655 eruption of Mt. Taranaki, New Zealand. *Journal of Volcanology and Geothermal Research*, **161**, 15–34, https://doi.org/10.1016/j.jvolgeores.2006.11.005

Plank, T., Kelley, K.A., Zimmer, M.M., Hauri, E.H. and Wallace, P.J. 2013. Why do mafic arc magmas contain *c.* 4 wt% water on average? *Earth and Planetary Science Letters*, **364**, 168–179, https://doi.org/10.1016/j.epsl.2012.11.044

Price, R.C., McCulloch, M.T., Smith, I.E.M. and Stewart, R.B. 1992. Pb–Nd–Sr isotopic compositions and trace element characteristics of young volcanic rocks from Egmont Volcano and comparisons with basalts and andesites from the Taupo Volcanic Zone, New Zealand. *Geochimica et Cosmochimica Acta*, **56**, 941–953, https://doi.org/10.1016/0016-7037(92)90038-K

Price, R.C., Stewart, R.B., Woodhead, J.D. and Smith, I.E.M. 1999. Petrogenesis of high-K arc magmas: evidence from Egmont Volcano, North Island, New Zealand. *Journal of Petrology*, **40**, 167–197, https://doi.org/10.1093/petroj/40.1.167

Price, R., Spandler, C., Arculus, R. and Reay, A. 2011. The Longwood Igneous Complex, Southland, New Zealand: a Permo-Jurassic, intra-oceanic, subduction-related, I-type batholithic complex. *Lithos*, **126**, 1–21, https://doi.org/10.1016/j.lithos.2011.04.006

Price, R.C., Mortimer, N., Smith, I.E.M. and Maas, R. 2015. Whole-rock geochemical reference data for Torlesse and Waipapa terranes, North Island, New Zealand. *New Zealand Journal of Geology and Geophysics*, **58**, 213–228, https://doi.org/10.1080/00288306.2015.1026832

Price, R.C., Smith, I.E.M., Stewart, R.B., Gamble, J.A., Gruender, K. and Maas, R. 2016. High-K andesite petrogenesis and crustal evolution: evidence from mafic and ultramafic xenoliths, Egmont Volcano (Mt. Taranaki) and comparisons with Ruapehu Volcano, North Island, New Zealand. *Geochimica et Cosmochimica Acta*, **185**, 328–357, https://doi.org/10.1016/j.gca.2015.12.009

Price, R.C., Cronin, S.J., Smith, I.E.M., Ukstins, I.A. and Zernack, A.V. 2021. Formation of crystal-rich, mixed, intermediate lavas at Pouakai Volcano and the evolution of the Taranaki volcanic lineament, western North Island, New Zealand. *Lithos*, **380–381**, 105850, https://doi.org/10.1016/j.lithos.2020.105850

Procter, J.N., Cronin, S.J. and Zernack, A.V. 2009. Landscape and sedimentary response to catastrophic debris avalanches, western Taranaki, New Zealand. *Sedimentary Geology*, **220**, 271–287, https://doi.org/10.1016/j.sedgeo.2009.04.027

Putirka, K.D. 2008. Thermometers and barometers for volcanic systems. *Reviews in Mineralogy and Geochemistry*, **69**, 61–120, https://doi.org/10.2138/rmg.2008.69.3

Putirka, K. 2016. Amphibole thermometers and barometers for igneous systems and some implications for eruption mechanisms of felsic magmas at arc volcanoes. *American Mineralogist*, **101**, 841–858, https://doi.org/10.2138/am-2016-5506

Reyners, M., Eberhart-Phillips, D., Stuart, G. and Nishimura, Y. 2006. Imaging subduction from the trench to 300 km depth beneath the central North Island, New Zealand, with *Vp* and *Vp*/*Vs*. *Geophysical Journal International*, **165**, 565–583, https://doi.org/10.1111/j.1365-246X.2006.02897.x

Ridolfi, F. and Renzulli, A. 2012. Calcic amphiboles in calc-alkaline and alkaline magmas: thermobarometric and chemometric empirical equations valid up to 1130°C and 2.2 GPa. *Contributions to Mineralogy and Petrology*, **163**, 877–895, https://doi.org/10.1007/s00410-011-0704-6

Salters, V.J.M. and Stracke, A. 2004. Composition of the depleted mantle. *Geochemistry, Geophysics, Geosystems*, **55**, https://doi.org/10.1029/2003GC000597

Shane, P., Cocker, K., Coote, A., Stirling, C. H. and Reid, M. R.2019). The prevalence of plagioclase antecrysts and xenocrysts in andesite magma, exemplified by lavas of the Tongariro volcanic complex, New Zealand. *Contributions to Mineralogy and Petrology*, **174**, 89, https://doi.org/10.1007/s00410-019-1626-y

Sherburn, S. and White, R.S. 2005. Crustal seismicity in Taranaki, New Zealand using accurate hypocentres from a dense network. *Geophysical Journal International*, **162**, 494–506, https://doi.org/10.1111/j.1365-246X.2005.02667.x

Sherburn, S., White, R.S. and Chadwick, M. 2006. Three-dimensional tomographic imaging of the Taranaki volcanoes, New Zealand. *Geophysical Journal International*, **166**, 957–969, https://doi.org/10.1111/j.1365-246X.2006.03040.x

Solano, J., Jackson, M., Sparks, R., Blundy, J. and Annen, C. 2012. Melt segregation in deep crustal hot zones: a mechanism for chemical differentiation, crustal assimilation and the formation of evolved magmas. *Journal of Petrology*, **53**, 1999–2026, https://doi.org/10.1093/petrology/egs041

Stern, T.A., Stratford, W.R. and Salmon, M.L. 2006. Subduction evolution and mantle dynamics at a continental margin: Central North Island, New Zealand. *Reviews of Geophysics*, **44**, RG4002, https://doi.org/10.1029/2005RG000171

Stern, T., Stratford, W. *et al.* 2010. Crust–mantle structure of the central North Island, New Zealand, based on seismological observations. *Journal of Volcanology and Geothermal Research*, **190**, 58–74, https://doi.org/10.1016/j.jvolgeores.2009.11.017

Stewart, R.B., Price, R.C. and Smith, I.E.M. 1996. Evolution of high-K arc magma, Egmont volcano, Taranaki, New Zealand: evidence from mineral chemistry. *Journal of Volcanology and Geothermal Research*, **74**, 275–295, https://doi.org/10.1016/S0377-0273(96)00049-2

Straub, S.M., Gomez-Tuena, A., Stuart, F.M., Zellmer, G.F., Espinasa-Perena, R., Cai, Y. and Iizuka, Y. 2011. Formation of hybrid arc andesites beneath thick continental crust. *Earth and Planetary Science Letters*, **303**, 337–347, https://doi.org/10.1016/j.epsl.2011.01.013

Straub, S.M., Gómez-Tuena, A. and Vannucchi, P. 2020. Subduction erosion and arc volcanism. *Nature Reviews Earth & Environment*, **1**, 574–589, https://doi.org/10.1038/s43017-020-0095-1

Torres-Orozco, R., Cronin, S.J., Damaschke, M. and Pardo, N. 2017. Diverse dynamics of Holocene mafic–intermediate Plinian eruptions at Mt. Taranaki (Egmont), New Zealand. *Bulletin of Volcanology*, **79**, 76, https://doi.org/10.1007/s00445-017-1162-4

Turner, M.B., Cronin, S.J., Bebbington, M.S. and Platz, T. 2008. Developing probabilistic eruption forecasts for dormant volcanoes: a case study from Mt Taranaki, New Zealand. *Bulletin of Volcanology*, **70**, 507–515, https://doi.org/10.1007/s00445-007-0151-4

Turner, M.B., Bebbington, M.S., Cronin, S.J. and Stewart, R.B. 2009*a*. Merging eruption datasets: building an integrated Holocene eruptive record for Mt Taranaki, New Zealand. *Bulletin of Volcanology*, **71**, 903–918, https://doi.org/10.1007/s00445-009-0274-x

Turner, S., Handler, M., Bindeman, I. and Suzuki, K. 2009*b*. New insights into the origin of O–Hf–Os isotope signatures in arc lavas from Tonga–Kermadec. *Chemical Geology*, **266**, 187–193, https://doi.org/10.1016/j.chemgeo.2009.05.027

Turner, M.B., Cronin, S.J., Bebbington, M.S., Smith, I.E.M. and Stewart, R.B. 2011. Integrating records of explosive and effusive activity from proximal and distal sequences: Mt. Taranaki, New Zealand. *Quaternary International*, **246**, 364–373, https://doi.org/10.1016/j.quaint.2011.07.006

Ubide, T., Galé, C., Arranz, E., Lago, M. and Larrea, P. 2014*a*. Clinopyroxene and amphibole crystal populations in a lamprophyre sill from the Catalonian Coastal Ranges (NE Spain): a record of magma history and a window to mineral–melt partitioning. *Lithos*, **184–187**, 225–242, https://doi.org/10.1016/j.lithos.2013.10.029

Ubide, T., Galé, C., Larrea, P., Arranz, E. and Lago, M.J.L. 2014*b*. Antecrysts and their effect on rock compositions: the Cretaceous lamprophyre suite in the Catalonian Coastal Ranges (NE Spain). *Lithos*, **206**, 214–233, https://doi.org/10.1016/j.lithos.2014.07.029

Ubide, T., Mollo, S., Zhao, J.-X., Nazzari, M. and Scarlato, P. 2019. Sector-zoned clinopyroxene as a recorder of magma history, eruption triggers, and ascent rates. *Geochimica et Cosmochimica Acta*, **251**, 265–283, https://doi.org/10.1016/j.gca.2019.02.021

Waters, L.E. and Lange, R.A. 2015. An updated calibration of the plagioclase–liquid hygrometer–thermometer applicable to basalts through rhyolites. *American Mineralogist*, **100**, 2172–2184, https://doi.org/10.2138/am-2015-5232

Wieser, P.E., Kent, A.J., Till, C., Donovan, J., Neave, D.A., Blatter, D. and Krawczynski, M.M. 2022. Barometers behaving badly: assessing the influence of analytical and experimental uncertainty on clinopyroxene thermobarometry calculations at crustal conditions. *Journal of Petrology*, **64**, egac126, https://doi.org/10.1093/petrology/egac126

Zellmer, G.F. 2021. Gaining acuity on crystal terminology in volcanic rocks. *Bulletin of Volcanology*, **83**, 78, https://doi.org/10.1007/s00445-021-01505-9

Zellmer, G.F., Pistone, M., Iizuka, Y., Andrews, B.J., Gomez-Tuena, A., Straub, S.M. and Cottrell, E. 2016. Petrogenesis of antecryst-bearing arc basalts from the Trans-Mexican Volcanic Belt: insights into along-arc variations in magma–mush ponding depths, H_2O contents, and surface heat flux. *American Mineralogist*, **101**, 2405–2422, https://doi.org/10.2138/am-2016-5701

Zernack, A.V. and Procter, J.N. 2021. Cyclic growth and destruction of volcanoes. *In*: Roverato, M., Dufresne, A. and Procter, J. (eds) *Volcanic Debris Avalanches*. Springer, 311–355, https://doi.org/10.1007/978-3-030-57411-6_12

Zernack, A.V., Procter, J.N. and Cronin, S.J. 2009. Sedimentary signatures of cyclic growth and destruction of stratovolcanoes: a case study from Mt. Taranaki, New Zealand. *Sedimentary Geology*, **220**, 288–305, https://doi.org/10.1016/j.sedgeo.2009.04.024

Zernack, A.V., Cronin, S.J., Neall, V.E. and Procter, J.N. 2011. A medial to distal volcaniclastic record of an andesite stratovolcano: detailed stratigraphy of the ring-plain succession of south-west Taranaki, New Zealand. *International Journal of Earth Sciences*, **100**, 1937–1966, https://doi.org/10.1007/s00531-010-0610-6

Zernack, A.V., Price, R.C., Smith, I.E.M., Cronin, S.J. and Stewart, R.B. 2012. Temporal evolution of a high-K andesitic magmatic system: Taranaki volcano, New Zealand. *Journal of Petrology*, **53**, 325–363, https://doi.org/10.1093/petrology/egr064